

Superconducting gap symmetry from Bogoliubov quasiparticle interference analysis on Sr_2RuO_4

Shinibali Bhattacharyya,¹ Andreas Kreisel,² X. Kong,³ T. Berlijn,³ Astrid T. Rømer,⁴ Brian M. Andersen,⁴ and P. J. Hirschfeld⁵

¹*Institut für Theoretische Physik, Goethe-Universität, 60438 Frankfurt am Main, Germany*

²*Institut für Theoretische Physik, Universität Leipzig, D-04103 Leipzig, Germany*

³*Center For Nanophase Materials Sciences, Oak Ridge National Laboratory, Oak Ridge, TN 37831, USA*

⁴*Niels Bohr Institute, University of Copenhagen,*

Rådmannsgade 62, DK-2200 Copenhagen, Denmark

⁵*Department of Physics, University of Florida, Gainesville, Florida 32611, USA*

(Dated: May 24, 2022)

The nature of the superconducting order parameter in Sr_2RuO_4 has generated intense interest in recent years. Since the superconducting gap is very small, high resolution methods such as scanning tunneling spectroscopy might be the best chance to directly resolve the gap symmetry. Recently, a Bogoliubov quasiparticle interference imaging (BQPI) experiment has suggested that the $d_{x^2-y^2}$ gap symmetry is appropriate for Sr_2RuO_4 . In this work, we use a more refined theoretical approach based on Wannier functions of the surface of Sr_2RuO_4 to calculate the continuum density of states as detected in scanning tunneling microscopy experiments. We examine several different proposed gap order parameters, and calculate the expected BQPI pattern for each case. Comparing to the available experimental data, our results suggest that a $s' + id_{xy}$ gap order parameter is the most probable state, but the measured BQPI patterns still display features unaccounted for by the theory for any of the states currently under discussion.

I. INTRODUCTION

Sr_2RuO_4 ^{1–4} has once again been a topic of intense research interest recently. For long time it was discussed as a promising candidate for intrinsic topological superconductor in the light of arguments in favor of a $p + ip$ symmetry of the gap order, in particular early evidence from NMR⁵. Muon-spin rotation⁶ and Kerr effect⁷ measurements were argued to imply time-reversal symmetry (TRS) breaking⁸ in the superconducting state, consistent with this picture. However, a number of thermodynamic measurements detected low-energy quasiparticle states, hinting at the existence of nodes or deep minima in the gap $\Delta(\mathbf{k})$ ^{9–12}.

Recently, strong evidence against the chiral p -wave paradigm was provided by in-plane ^{17}O nuclear magnetic resonance measurements^{13,14} that found a substantial drop in the Knight shift below T_c . Arguments in favor of spin singlet pairing were then drawn from the field dependence of the Knight shift in comparison to the change of the entropy from earlier specific heat experiments¹⁵. These measurements are complemented by observations of shifts in the elastic constants^{16,17} together with experiments under strain¹⁸ that indicate a two component nature of the order parameter. All these findings have led to a series of recent theoretical attacks on the question of superconductivity in Sr_2RuO_4 ^{19–32}.

Sr_2RuO_4 is generally considered to be an unconventional superconductor, where electron pairing is mediated by the exchange of electronic excitations, so theories typically attempt to model the low-energy effective pairing interaction. The Fermi surface is dominated by three Ru d orbitals d_{xz}, d_{yz} that contribute mostly to quasi-1D bands, and d_{xy} states dominating a

2D band. Electrons in these states interact via intrasite Coulomb U interactions and Hund's coupling J , with the d_{xy} dominant bands thought to be more strongly correlated.^{33,34} In addition, spin-orbit coupling plays a significant role^{35,36}. Recent microscopic theories incorporate many of these ingredients^{19–21,25,26,29,37,38}, leading to a variety of predictions for $\Delta(\mathbf{k})$ depending on details, and other symmetries have been proposed on purely phenomenological grounds^{23,24,30}. These predictions include various 1D spin singlet irreducible representations, e.g. $B_{1g}(d_{x^2-y^2})$, as well as 2D singlet states $E_{1g}(d_{xz} + id_{yz})$, and A_{1u} (helical p) symmetry as well as more complex triplet orders^{19–21}. A two-component state is generally thought to be important to explain the observation of time-reversal symmetry breaking, ultrasound^{17,39}, and recent μSR experiments under strain¹⁸. At zero strain, these can in principle correspond either to the 2D representations, or to accidental degeneracies of two 1D representations.

Not all such proposals are consistent with existing experimental results, nor are all the interpretations of the experimental literature apparently consistent with one another⁴. In such a situation it would be extremely useful to have a direct measurement of the superconducting gap to distinguish among theories and thereby constrain the possible pairing mechanisms. The extremely small size ($|\Delta| \leq 350 \mu\text{eV}$)^{40,41} of the superconducting order parameter $\Delta(\mathbf{k})$ in Sr_2RuO_4 has hindered such measurements for a long time, as they require low temperatures and fine energy resolution to detect spectral features arising from the small gap. However, in principle Bogoliubov quasiparticle interference (BQPI) imaging is a powerful technique capable of high-precision measurement of multiband $\Delta(\mathbf{k})$ ^{42–44}. Interference of impurity-scattered

quasiparticles produces real space Friedel oscillations in the density of states (DOS) $\rho(\mathbf{r}, \omega)$ within the energy range of $\Delta(\mathbf{k})$, giving rise to complex patterns in the spatial Fourier transform spectrum $\rho(\mathbf{q}, \omega)$ that can in principle be measured in an STM experiment and interpreted in order to extract the gap structure. The BQPI technique was recently implemented to analyze $\Delta(\mathbf{k})$ in Sr_2RuO_4 ⁴¹. This analysis, motivated with observations from recent work^{12,13,19–21,45}, suggested a $d_{x^2-y^2}$ superconducting gap symmetry for Sr_2RuO_4 by comparison with theoretical calculations of $\rho(\mathbf{q}, \omega)$ using simple low-harmonic gap candidates $\Delta(\mathbf{k})$. Such an approach is, however, limited by a) loss of \mathbf{q} space resolution when calculating BQPI on a simple Ru lattice system; b) failure to include the rather complex gap structures, including accidental nodes, anticipated by microscopic theories^{19,29}.

In this work, we will adopt the Wannier-based T -matrix technique introduced in Refs. [46 and 47] through which one obtains BQPI images for real materials in its normal and superconducting states, that are directly comparable to experiments. Unlike the theoretical approach used in Ref. [41] to obtain lattice DOS $\rho(\mathbf{R}, \omega)$, the Wannier-based T -matrix approach is used for evaluation of the continuum DOS $\rho(\mathbf{r}, \omega)$ dressed by real-space Wannier functions pertaining to the orbitals that have dominant contribution around the Fermi level of the material under consideration. These Wannier functions substantially modify the continuum DOS patterns, bringing in additional $\mathbf{q}(\omega)$ features in its Fourier transformed image. In addition, we take as representative of the various possible gap symmetries not only simple harmonics, but gaps derived from microscopic spin fluctuation pairing theory²⁹. We find that definitive conclusions are difficult because of limited experimental data and the fact that BQPI features are remarkably non-dispersive in this system, even for highly anisotropic gap structures. The best fit to the data currently available⁴¹ suggests a $s' + id_{xy}$ gap order parameter, but we discuss other alternatives in detail.

This paper is organized as follows: in Section II, we introduce the multiorbital Hubbard Hamiltonian with the pairing and impurity terms, and describe it using the Bardeen-Cooper-Schrieffer (BCS) equations in the Nambu spinor basis. We write down the equations for computing the lattice DOS and continuum DOS^{46,47}, in the presence of impurities using the T-matrix approach. In Section III, we demonstrate our BQPI findings first in the normal state, and second in the superconducting state of the material for which we borrow the singlet and composite gap order parameters as obtained in Refs. [19 and 29]. Finally, we present our conclusions in Section IV and possible future directions of investigation in this context.

II. MODEL

In this section, we will lay out the theoretical framework on how the surface of a material is imaged by STM. The full Hamiltonian has four terms, namely the kinetic energy term H_0 , the spin-orbit term H_{soc} , the BCS like interaction term H_{BCS} and a single-impurity term H_{imp} .

$$H = H_0 + H_{\text{soc}} + H_{\text{MF}} + H_{\text{imp}}, \quad (1)$$

$$H_0 = \sum_{\mathbf{R}\mathbf{R}'mn} t_{\mathbf{R}\mathbf{R}'}^{mn} c_{\mathbf{R}ms}^\dagger c_{\mathbf{R}'ns} - \mu_0 \sum_{\mathbf{R}ms} c_{\mathbf{R}ms}^\dagger c_{\mathbf{R}ms},$$

$$H_{\text{MF}} = - \sum_{\mathbf{R}\mathbf{R}'mn} [\Delta_{\mathbf{R}\mathbf{R}'}^{mn} c_{\mathbf{R}m\uparrow}^\dagger c_{\mathbf{R}'n\downarrow}^\dagger + h.c.],$$

$$H_{\text{imp}} = \sum_{\mathbf{R}^*mns} V_{\text{imp}}^{mn} c_{\mathbf{R}^*ms}^\dagger c_{\mathbf{R}^*ns}.$$

H_{soc} will be introduced in the next subsection. Here, $c_{\mathbf{R}ms}^\dagger$ ($c_{\mathbf{R}ms}$) is the creation (annihilation) operator for an electron in the unit cell \mathbf{R} , orbital m with spin s . $t_{\mathbf{R}\mathbf{R}'}^{mn}$ is the amplitude for hopping from unit cell \mathbf{R} , orbital m to the unit cell \mathbf{R}' , orbital n . The pairing field is given by $\Delta_{\mathbf{R}\mathbf{R}'}^{mn} = V_{\mathbf{R}\mathbf{R}'}^{mn} \langle c_{\mathbf{R}'n\downarrow} c_{\mathbf{R}m\uparrow} \rangle$, where $V_{\mathbf{R}\mathbf{R}'}^{mn}$ is the effective attraction between unit cell \mathbf{R} , orbital m and unit cell \mathbf{R}' , orbital n . \mathbf{R}^* is the impurity site and V_{imp}^{mn} is the (on-site only) non-magnetic impurity potential responsible for scattering of quasiparticles.

A. Non-interacting Hamiltonian

We will adopt the non-interacting tight-binding Hamiltonian model for Sr_2RuO_4 as used in Refs. [19, 27, and 29]. It is composed of the three Ru orbitals: d_{xz} , d_{yz} and d_{xy} . Fourier transforming the real space hoppings from H_0 fitted to ARPES measurements^{48,49}, one obtains the dispersions given by $\xi_{xz}(\mathbf{k}) = -2t_1 \cos k_x - 2t_2 \cos k_y - \mu$, $\xi_{yz}(\mathbf{k}) = -2t_2 \cos k_x - 2t_1 \cos k_y - \mu$, and $\xi_{xy}(\mathbf{k}) = -2t_3(\cos k_x + \cos k_y) - 4t_4 \cos k_x \cos k_y - 2t_5(\cos 2k_x + \cos 2k_y) - \mu$ with $\{t_1, t_2, t_3, t_4, t_5\} = \{88, 9, 80, 40, 5, 109\}$ meV with the inter-orbital hybridization $g(\mathbf{k})$ set to 0 (see Eq.2 below) and the chemical potential $\mu = 109$ meV. Atomic SOC is parametrized by $H_{\text{soc}} = \lambda_{\text{soc}} \mathbf{L} \cdot \mathbf{S}$ and gives rise to orbital mixing on the Fermi surface sheets. We include SOC of $\lambda_{\text{soc}} \approx 40$ meV ($\approx 0.5t_1$)^{19,27,29}. For the TRS-preserved normal state, we have doubly degenerate Kramer's eigenvalues and the non-interacting Hamiltonian \hat{H} in block-diagonal form can be represented in a pseudospin basis $\sigma = +(-)$. Here $\hat{H} = \sum_{\mathbf{k}\sigma} \Psi^\dagger(\mathbf{k}, \sigma) (H_0 + H_{\text{soc}}(\sigma)) \Psi(\mathbf{k}, \sigma)$ where,

$$H_0 = \begin{pmatrix} \xi_{xz}(\mathbf{k}) & g(\mathbf{k}) & 0 \\ g(\mathbf{k}) & \xi_{yz}(\mathbf{k}) & 0 \\ 0 & 0 & \xi_{xy}(\mathbf{k}) \end{pmatrix} \quad (2)$$

$$H_{\text{soc}}(\sigma) = \frac{1}{2} \begin{pmatrix} 0 & -i\sigma\lambda_{\text{soc}} & i\lambda_{\text{soc}} \\ i\sigma\lambda_{\text{soc}} & 0 & -\sigma\lambda_{\text{soc}} \\ -i\lambda_{\text{soc}} & -\sigma\lambda_{\text{soc}} & 0 \end{pmatrix} \quad (3)$$

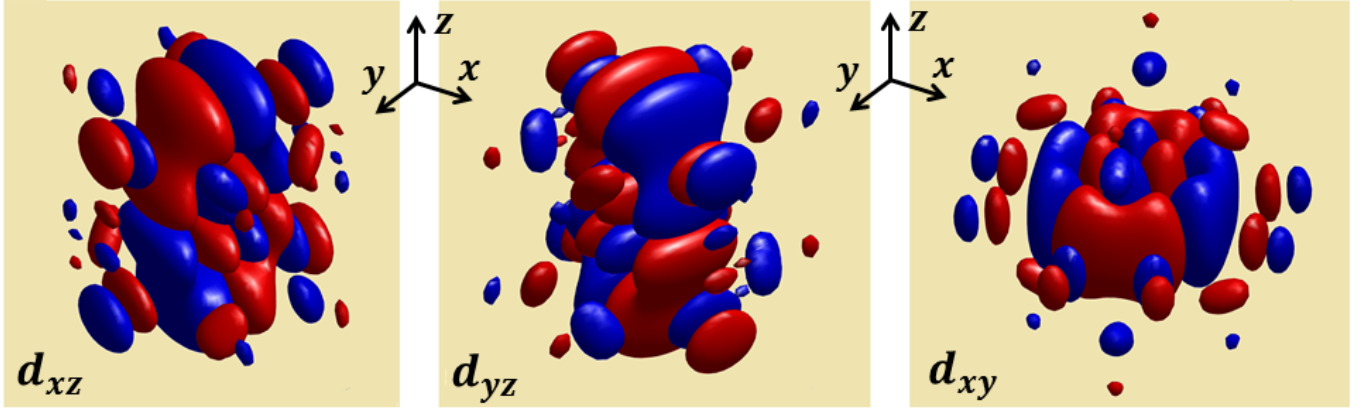


FIG. 1. Isosurface plots of d_{xz} , d_{yz} and d_{xy} Ru Wannier orbitals in Sr_2RuO_4 . Red and blue colors indicate the opposite phases of the wave function.

and $\Psi(\mathbf{k}, +) = [c_{xz\uparrow}(\mathbf{k}), c_{yz\uparrow}(\mathbf{k}), c_{xy\downarrow}(\mathbf{k})]^T$ and $\Psi(\mathbf{k}, -) = [c_{xz\downarrow}(\mathbf{k}), c_{yz\downarrow}(\mathbf{k}), c_{xy\uparrow}(\mathbf{k})]^T$.

B. Superconducting gap

The superconducting gap in momentum space in the homogeneous system is obtained from the spin-fluctuation pairing theory evaluations^{19,29}. The full BCS Hamiltonian (implied by the underscore) is given by:

$$\hat{H} = \begin{pmatrix} \hat{H}(\mathbf{k}) & \hat{\Delta}(\mathbf{k}) \\ \hat{\Delta}^\dagger(\mathbf{k}) & -\hat{H}^T(-\mathbf{k}) \end{pmatrix}, \quad (4)$$

written in the Nambu spinor basis $(\Phi^\dagger(\mathbf{k}), \Phi^T(-\mathbf{k}))$ where $\Phi^\dagger(\mathbf{k}) = (\Psi^\dagger(\mathbf{k}, +), \Psi^\dagger(\mathbf{k}, -))$. Diagonalizing \hat{H} yields the eigenvalues $\{\pm E_\mu(\mathbf{k})\}$ and the unitary transformation matrix $\hat{U}(\mathbf{k})$ that diagonalizes \hat{H} . The orbitally resolved-gap structure $\hat{\Delta}^{mn}(\mathbf{k})$ is also expressed in this Nambu basis⁴⁷ [see Appendix B for theoretical details]. We evaluate six different cases of pseudo-spin-singlet ($|\uparrow\downarrow\rangle - |\downarrow\uparrow\rangle$) gap order parameters: simple intra-band $d_{x^2-y^2}^S$ where $\hat{\Delta}_\mu(\mathbf{k}) = \frac{\Delta_0}{2}(\cos k_x - \cos k_y)$, and the rest taken from Refs. [19 and 29] $d_{x^2-y^2}$, s' , $s' + id_{x^2-y^2}$ and $s' + id_{xy}$.

The orbitally-resolved homogeneous DOS in the superconducting state is $\rho^n(\omega) = -\frac{1}{\pi}\text{Im} \sum_{\mathbf{k}} \hat{G}_{nn}(\mathbf{k}, \omega)$ where

$$\hat{G}(\mathbf{k}, \omega) = (\omega - \hat{H}(\mathbf{k}) + i\delta)^{-1}, \quad (5)$$

is the Green's function for the BCS Hamiltonian. The real-space bare lattice Green's function is obtained from the Fourier transform

$$\hat{G}^0(\mathbf{R}, \mathbf{R}', \omega) = \sum_{\mathbf{k}} e^{-i\mathbf{k}\cdot(\mathbf{R}-\mathbf{R}')} \hat{G}^0(\mathbf{k}, \omega) = \hat{G}^0(\mathbf{R} - \mathbf{R}', \omega). \quad (6)$$

C. Impurity states and T-matrix approach

With intra-orbital, on-site impurity potential terms V_{imp}^{nn} in H_{imp} of Eq. (1), one constructs the lattice Green's function in the presence of the impurity via the T-matrix approach:

$$\underline{\hat{G}}(\mathbf{R}, \mathbf{R}', \omega) = \underline{\hat{G}}^0(\mathbf{R} - \mathbf{R}', \omega) + \underline{\hat{G}}^0(\mathbf{R}, \omega) \underline{T}(\omega) \underline{\hat{G}}^0(-\mathbf{R}', \omega). \quad (7)$$

The T-matrix is given by

$$\underline{\hat{T}}(\omega) = [\mathbb{1} - \underline{\hat{V}}_{\text{imp}} \underline{\hat{G}}(\omega)]^{-1} \underline{\hat{V}}_{\text{imp}}, \quad (8)$$

where the local Green's function is $\hat{G}(\omega) = \sum_{\mathbf{k}} \hat{G}(\mathbf{k}, \omega)$ and the diagonal matrix $\underline{\hat{V}}_{\text{imp}} = V_{\text{imp}}^{mn} \delta_{mn} \underline{\tau}_z$, implying its expression in the Nambu spinor basis with

$$\underline{\tau}_z = \begin{pmatrix} \mathbb{1} & 0 \\ 0 & -\mathbb{1} \end{pmatrix}. \quad (9)$$

D. Wannier functions to calculate continuum density of states

For a given bias voltage V , the differential tunneling conductance in an STM experiment is given by⁵⁰:

$$\frac{dI}{dV}(\mathbf{r}, eV) = \frac{4\pi e}{\hbar} |M|^2 \rho_{\text{tip}}(0) \rho(\mathbf{r}, eV), \quad (10)$$

where $\mathbf{r} = (x, y, z)$ denote the coordinates of the tip, $\rho(\mathbf{r}, eV)$ is the continuum LDOS (cLDOS), $\rho_{\text{tip}}(0)$ is the DOS of the tip, and $|M|^2$ is the square of the matrix element for the tunneling barrier. The following methodology to include the effect of Wannier functions in modifying the cLDOS was introduced in Refs. 46 and 47. The cLDOS can be calculated by

$$\rho(\mathbf{r}, \omega) = -\frac{1}{\pi} \text{Im} G^{11}(\mathbf{r}, \mathbf{r}, \omega), \quad (11)$$

where $G^{11}(\mathbf{r}, \mathbf{r}, \omega) = \sum_s G_{ss}(\mathbf{r}, \mathbf{r}, \omega)$ is the normal part of the Nambu continuum Green's function defined in a basis described by the field operators $\psi_s(\mathbf{r})$. These are related to the lattice operators $c_{\mathbf{R}ms}$ through the Wannier functions matrix elements $w_{\mathbf{R}m}(\mathbf{r})$ as $\psi_s(\mathbf{r}) = \sum_{\mathbf{R}m} c_{\mathbf{R}ms} w_{\mathbf{R}m}(\mathbf{r})$. Employing the Wannier basis transformation^{46,47}, we can obtain the continuum Green's function as:

$$G_{ss'}(\mathbf{r}, \mathbf{r}', \omega) = \sum_{\mathbf{R}\mathbf{R}'mn} \hat{G}_{ms,ns'}(\mathbf{R}, \mathbf{R}', \omega) w_{\mathbf{R}m}(\mathbf{r}) w_{\mathbf{R}'n}(\mathbf{r}') \quad (12)$$

and thereafter, evaluate the cLDOS from Eq. (11). A simple Fourier transform of the cLDOS $\rho(\mathbf{r}, \omega)$ gives the Bogoliubov quasiparticle interference maps that can be compared directly to experimental measurements.

III. RESULTS

Sr_2RuO_4 crystal structure is composed of alternating layers of SrO and RuO_2 planes. The cleaving of the sample in ultrahigh vacuum at low temperatures is considered to reveal atomically flat SrO cleaved surface⁴¹. However, an STM tip probing this surface is believed to be sensitive to the atomic wave functions of the Ru d -orbitals that dominate the Fermi level, while the other atomic wave functions away from the Fermi level are effectively invisible for STM. An illustration of the Ru d -orbitals Wannier functions [as obtained from *ab-initio* calculations described in Appendix A] is provided in Fig.1. Notice the smaller z -expansions of the d_{xy} Wannier orbitals compared to d_{xz} , d_{yz} orbitals, making d_{xy} orbital less likely to participate in tunneling through an STM tip located at a certain z -height above the cleaved surface, a property that might be altered on reconstructed surfaces which do not show superconductivity⁵¹.

A. Homogeneous superconducting state

Figure 2(a) shows the Fermi surface (FS) for 2D Sr_2RuO_4 with the corresponding dominant orbital contribution. There are three FS pockets: two quasi-1D bands that originate from Ru d_{xz} (purple) and d_{yz} (yellow) orbitals, leading to the electron-like β band centered at the Γ point and hole-like α band surrounding the M point; and the Ru d_{xy} (blue) orbital generates the electron-like quasi-2D γ band centered at the Γ point. SOC lifts degeneracy of the β and γ bands along the diagonals in the first Brillouin zone and introduces further inter-orbital hybridization as seen in Fig.2(a).

Figure 3 shows the orbitally-resolved homogeneous DOS $\rho^n(\omega)$ in the superconducting state, with degenerate contributions from d_{xz} and d_{yz} orbitals depicted by the dark-yellow line and d_{xy} orbital contribution in blue. Results are presented for 6 different spin-singlet gap order parameters: (a) purely intra-band $d_{x^2-y^2}^S$ parameter

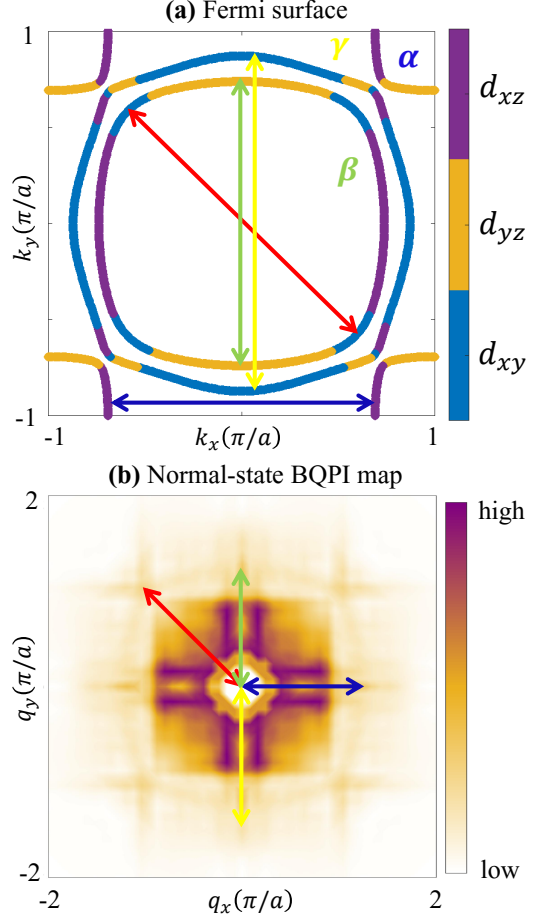


FIG. 2. (a) Fermi surface of Sr_2RuO_4 for the model discussed in Sec. II A with patches showing the dominant orbital content (d_{xz} , d_{yz} or d_{xy}) as indicated by the color legend. The normal state intra-band scattering vectors connecting patches with similar orbital character is indicated by red, green, yellow and blue arrows. (b) The QPI pattern for an impurity potential $V_{\text{imp}} = 0.05$ eV and for $\omega = 0$ eV in the normal state of the system. The \mathbf{q} -vectors corresponding to these red, green, yellow and blue arrows as shown in (a) are highlighted as well. Intensities in the central region surrounding $\mathbf{q} = (0, 0)$ have been suppressed to avoid visual bias.

as $\frac{\Delta_0}{2}(\cos k_x - \cos k_y)$, and the rest adapted from Refs. [19 and 29] (b) $d_{x^2-y^2}$, (c) s' , (d) $s' + id_{x^2-y^2}$, (e) $s' + id_{xy}$ and (f) $d_{x^2-y^2} + ig_{xy}(x^2 - y^2)$. While the gap functions (b)-(f) correspond to specific cases of microscopic parameters discussed in those references, it was shown there that their structure was reasonably robust against changes of those parameters within reasonable ranges. Thus we hope therefore to identify qualitative BQPI structures that are driven by these features. Case (a) with $d_{x^2-y^2}^S$ order parameter was evaluated to compare directly with the BQPI analysis claims of Ref. [41]. The gap maximum value for all cases was chosen as $\Delta_0 = 3.5$ meV, as required with the \mathbf{k} -grid size employed. A lower value of Δ_0 would require a larger \mathbf{k} -grid size for converged calculations; we verified that the qualitative features of

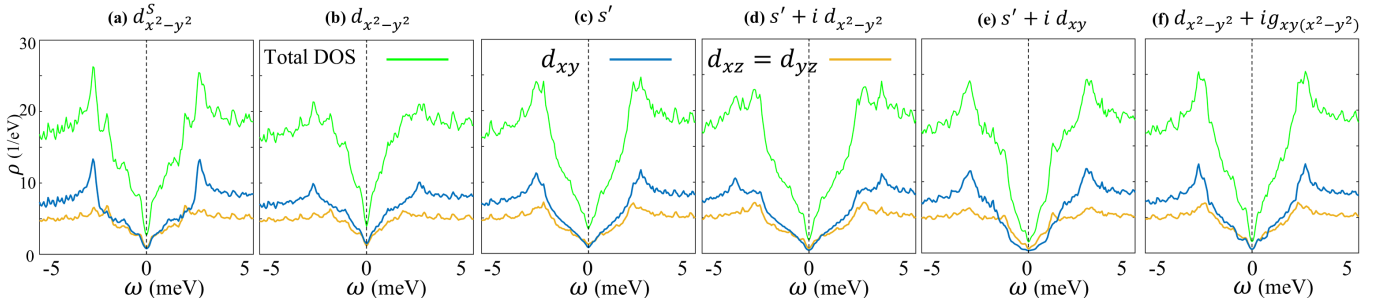


FIG. 3. Homogeneous orbitally-resolved DOS in the superconducting state for six different gap order parameters: (a) $d_{x^2-y^2}^S$ which is a simple intra-band order parameter of $\frac{\Delta_0}{2}(\cos k_x - \cos k_y)$, and the rest taken from Refs. [19 and 29] (b) $d_{x^2-y^2}$, (c) s' , (d) $s' + id_{x^2-y^2}$, (e) $s' + id_{xy}$ and (f) $d_{x^2-y^2} + ig_{xy}(x^2-y^2)$. Notice the V-shaped DOS spectrum across all cases.

computed BQPI patterns were robust against changes in the \mathbf{k} -grid.

The gap functions studied here all possess nodes or extremely deep near-nodes on the Fermi surface^{19,29}, such that spectra in Fig. 3 are all roughly V-shaped, consistent with STM measurements^{41,52}. Certain small features related to the multiband character of Sr_2RuO_4 are clearly visible, however. One can clearly identify the coherence peaks appearing in the vicinity of $\Delta_0 = \pm 3.5$ meV. Although some cases, particularly (e) with $s' + id_{xy}$ order parameter, show evidence of shoulders in the DOS at energies less than Δ_0 , this is not captured in experiments possibly due to: (1) the extremely low STM-bias resolution required to differentiate such a feature occurring below $\pm 350 \mu\text{eV}$ in the real system, and (2) smoothing of the DOS spectrum due to convolution with Fermi distribution function at finite temperatures as measured in the dI/dV spectrum⁵⁰. We have used 1000×1000 \mathbf{k} -grid and a broadening parameter of 0.1 meV for the above calculations.

B. Inhomogeneous superconducting state

To consider scattering from a single point-like impurity, we introduce an impurity substituting one of the atoms in the center of the cleaved surface and calculate the cLDOS over an area of 51×51 lattice constants. We consider a weak non-magnetic impurity scatterer that is purely intra-orbital, and diagonal in spin space, i.e. $(V_{\text{imp}}^{nn})_{ss} = 0.05 \text{ eV}$ appearing in Eq. (8). Modeling the disorder is the most uncertain part of this analysis, since we do not have microscopic knowledge of the sources of scattering. We therefore follow the simplest path by modeling impurities by a single δ -function with a potential chosen to best reproduce the simpler normal state QPI pattern. We therefore evaluate the Wannier function-modified cLDOS pattern obtained from Eq. (11), first, for the normal state and next, for the superconducting states discussed under cases (a-f) in Sec. III A. The spatial cLDOS is calculated on the xy -plane at a specific z -height above the cleaved surface of the sample (here,

$z = 5.7 \text{ \AA}$ is used for the Wannier functions). The specific choice of V_{imp} produces the QPI map of the normal state scattering processes at $\omega = 0 \text{ eV}$ as shown in Fig. 2(b) and shows qualitative agreement with experimental results of Ref.[41 and 53]. The normal state intra-band scattering vectors connecting FS patches with similar orbital character are indicated by the red, green, yellow and blue arrows in Fig. 2(a). These specific \mathbf{q} -vectors are highlighted in Fig. 2(b). One can notice less-intense \mathbf{q} -feature corresponding to the suppressed tunneling matrix elements for d_{xy} orbitals indicated by the yellow arrow.

Next, we discuss the results for BQPI maps obtained in the superconducting state as shown in Fig. 4 for cases (a-f). The top row shows the experimental BQPI data⁴¹ obtained at four different STM bias values $|\omega|$ expressed in units of the experimentally observed gap-maxima $\Delta = 350 \mu\text{eV}$. These values correspond to: $|\omega|/\Delta = [0, 0.26, 0.58, 0.84]$. The most consistently noticeable $\mathbf{q}(\omega)$ -features across all bias values are encircled in red, green, blue and yellow circles. Small $|\mathbf{q}|$ -features in the experiments are believed to be due to long-range disorder/drift in real space rather than any scattering interference, and hence, are removed from the plots. We compared these specific features appearing in our theoretically evaluated BQPI maps corresponding to the six different singlet and composite order parameters.

Before proceeding, we note one salient aspect of the application of the BQPI technique to SRO and other low- T_c unconventional superconductors. While we have emphasized the utility of the technique to provide information on the gap structure in superconductors with low T_c , such systems often have much larger Dirac cone anisotropies $v_F/v_\Delta \sim E_F/\Delta_0$ than, e.g., cuprates or Fe-based superconductors. As can be seen in the experimental data, there is therefore virtually no dispersion of the BQPI peak positions in the superconducting state, although the weights of these peaks change with bias. Colloquially, this is because the contours of constant quasiparticle energy are arcs rather than “bananas”. The dispersion takes place over a much smaller, and probably unresolvable range of \mathbf{q} . An analysis based on an analogue of the “octet” model applied to cuprates⁵⁴ is therefore

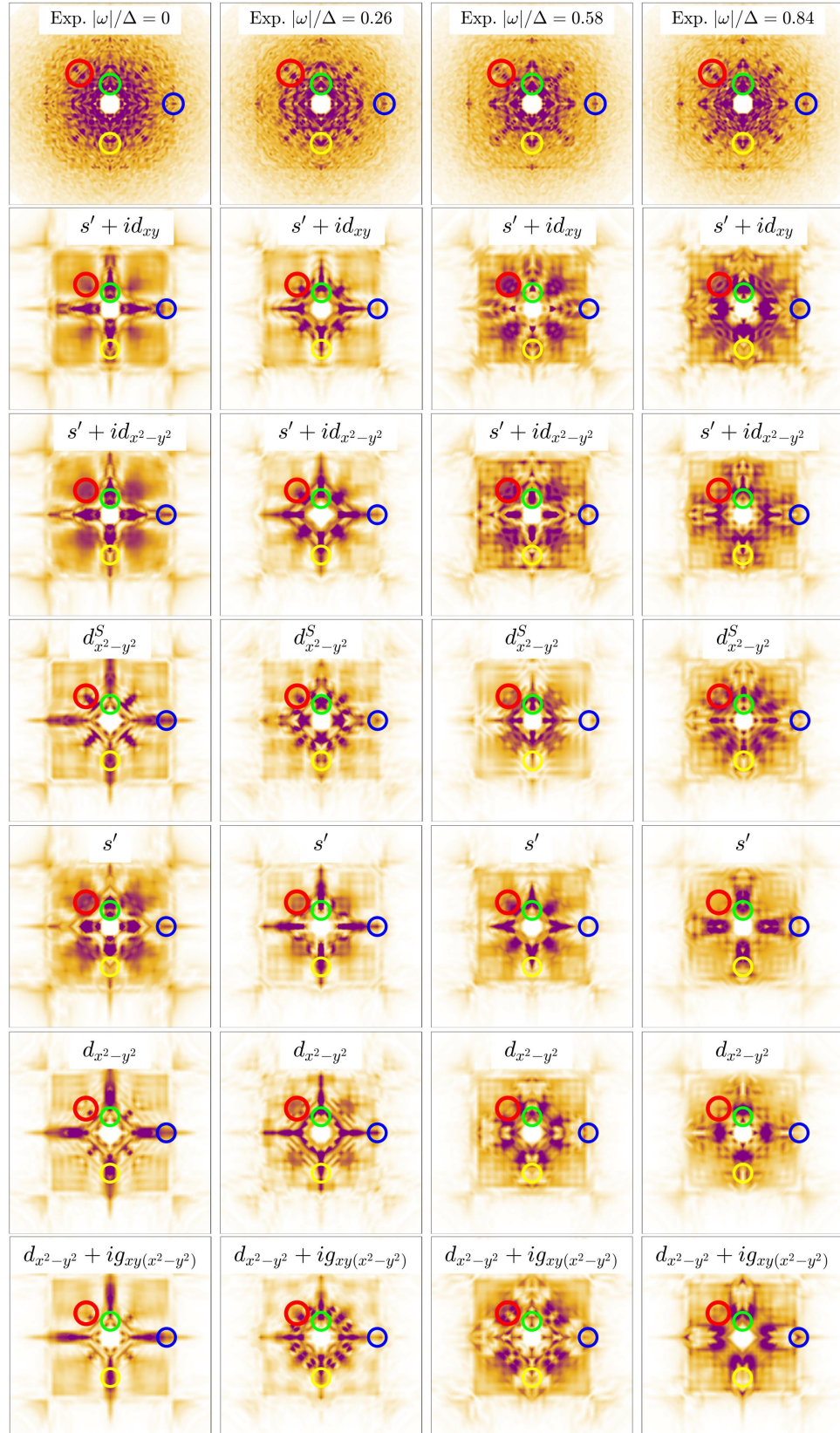


FIG. 4. BQPI maps obtained in the superconducting state from: (top row) experimental data⁴¹ obtained at four different STM bias values $|\omega|/\Delta = [0, 0.26, 0.58, 0.84]$ as marked for each column, followed by our theoretical predictions for (second row) $s' + id_{xy}$, (third) $s' + id_{x^2 - y^2}$, (fourth) $d_{x^2 - y^2}^S$, (fifth) s' , (sixth) $d_{x^2 - y^2}$ and (seventh) $d_{x^2 - y^2} + ig_{xy(x^2 - y^2)}$. Darker color denotes stronger intensity features. The most noticeable \mathbf{q} -features across all bias values are encircled in red, green, blue and yellow circles. The subsequent rows are arranged in a descending order starting from the case showing the most to the least consistency with the experimental patterns. Intensities in the central region surrounding $\mathbf{q} = (0, 0)$ have been suppressed to avoid visual bias. $|\omega|$ is expressed in units of the experimentally observed gap-maxima $\Delta = 350 \mu\text{eV}$ for the first row (or theoretically observed coherence peak values for subsequent rows).

not possible, eliminating one of the most powerful tools to identify the gap structure from BQPI.

We are therefore limited to comparing theoretical and experimental QPI maps at different biases and attempting to identify the most qualitatively robust features. In Fig.4, we arranged the rows of BQPI maps below the experimental data (first row) in a descending order starting from the case showing the most to the least consistency with the experimental patterns, i.e., second row for $s' + id_{xy}$, third for $s' + id_{x^2-y^2}$, fourth for $d_{x^2-y^2}^S$, fifth for s' , sixth for $d_{x^2-y^2}$ and seventh for $d_{x^2-y^2} + ig_{xy(x^2-y^2)}$. In other words, the BQPI pattern for $s' + id_{xy}$ order parameter shows strong peaks at the 4 \mathbf{q} -positions of the colored circles across all bias values, whereas $d_{x^2-y^2} + ig_{xy(x^2-y^2)}$ order parameter shows the least correspondence with these 4 specific \mathbf{q} -features. These 4 \mathbf{q} -positions were first identified from their ubiquitous and robust presence across all bias values in the experimental BQPI maps, and thereafter, their corresponding presence in the theoretically predicted BQPI maps were investigated. Furthermore, each pattern within a specific colored circle was scrutinized to its subtle details, to quantify a match between the experiment and the prediction. For instance, at STM bias of $\omega/\Delta = 0.84$, the pattern within red circle for $s' + id_{xy}$ data shows diagonal stripes similar to the experiment, hence, is assigned a score of 1; whereas the pattern within the red circle for $s' + id_{x^2-y^2}$ data shows stripes along x and y-direction and is assigned a score of 0. This analysis was carefully carried out for all the 4 STM biases across all the different gap order parameters and for all the 4 colored circles. A summary (score chart) of this correspondence is quantified in Table I below and a more detailed description is given in Appendix C. Additionally, the experimental features at higher STM biases $|\omega|/\Delta = [0.58, 0.84]$ show enhanced intensities along the square edges positioned around $(\pm 1.5\pi/a)$, as opposed to the lower biases $|\omega|/\Delta = [0, 0.26]$. This trend is also observed in the BQPI maps for the $s' + id_{xy}$ and the $s' + id_{x^2-y^2}$ order parameters, whereas the other order parameters tend to exhibit this feature at other bias values, not aligning with this trend. This enhanced square feature is believed to be arising from increased scattering between gradually re-appearing normal-state-like Bogoliubov contours at higher bias values.

As discussed in Ref.[41], the $d_{xz/yz}$ dominated α, β bands are detected from the normal-state scattering interference wave-vectors (blue, green and red arrows in Fig. 2 (a)) and subsequently, yield prominent signatures in the superconducting state. Under the knowledge that our gap order parameter exhibits multiple nodes and/or minima in the vicinity of $(\pm\pi/a, \pm\pi/a)$ on α, β, γ bands, there could be numerous scattering wave-vectors connecting these \mathbf{k} -regions. This gives rise to the rich and intricate BQPI patterns as observed in experiment and in our theoretical evaluations as well. However, we note that the most significant features highlighted by the red, green, blue and yellow circles (in Fig.4) correspond to major

scattering wave-vectors connecting the Bogoliubov contours along the $(\pm\pi/a, \pm\pi/a)$ on α, β, γ bands⁴¹. Detecting BQPI intensities at these specific \mathbf{q} vectors serves as a direct evidence for a superconducting gap structure with gap minima/nodes along $(\pm\pi/a, \pm\pi/a)$ on the different bands of Sr_2RuO_4 . The $s' + id_{xy}$ gap order parameter already contains these prominent features in addition to other features consistent with the experimental measurement.

Gap order	$ \omega /\Delta = 0$	$ \omega /\Delta = 0.26$	$ \omega /\Delta = 0.58$	$ \omega /\Delta = 0.84$	Total score
$s' + id_{xy}$	4/4	3/4	3/4	4/4	14/16
$s' + id_{x^2-y^2}$	2/4	2/4	4/4	3/4	11/16
$d_{x^2-y^2}^S$	3/4	4/4	2/4	2/4	11/16
s'	3/4	2/4	2/4	2/4	9/16
$d_{x^2-y^2}$	3/4	2/4	2/4	1/4	8/16
$d_{x^2-y^2} + ig_{xy(x^2-y^2)}$	2/4	2/4	2/4	2/4	8/16

TABLE I. Score chart summarizing the correspondence of the four specific \mathbf{q} -features at the colored circles (see Fig.4) between experimental and theoretically evaluated BQPI maps, for various gap order parameters across all STM biases $|\omega|/\Delta$. The fraction denotes the number of features that appear to coincide exactly within the 4 colored circles in each maps. The cumulative total score out of 16 \mathbf{q} -features (4 \mathbf{q} -features across 4 bias values) determines the ranking for the correspondence of the individual gap order parameters when matched with experimental BQPI patterns.

IV. SUMMARY

We have performed 2D calculations of the real-space Wannier function-modified continuum electronic density of states for Sr_2RuO_4 . Using the T-matrix approach in combination with Wannier functions for analyzing scattering effects from a single impurity point, we evaluated the real-space tunneling conductance map and displayed its Fourier transformed BQPI image to compare with STM measurements⁴¹. We have shown our evaluations for six possible pseudo-spin singlet and composite gap order parameters: (a) purely intra-band $d_{x^2-y^2}^S$ parameter ($\frac{\Delta_0}{2}(\cos k_x - \cos k_y)$), and the rest borrowed from Ref. [19 and 29]: (b) $d_{x^2-y^2}$, (c) s' , (d) $s' + id_{x^2-y^2}$, (e) $s' + id_{xy}$, and (f) $d_{x^2-y^2} + ig_{xy(x^2-y^2)}$. We compared the important features between our theoretical predictions and the experimental measurements for the homogeneous DOS spectrum and the BQPI patterns, and concluded that the $s' + id_{xy}$ gap order parameter seems to be the most consistent with our observations. Since the analysis of BQPI patterns is a classic example of “pattern recognition” problem⁵⁵, future investigations in this context can be directed towards training convolutional neural networks with theoretically generated images of BQPI patterns labeled for various STM biases and gap order

parameters, and testing them on experimental data sets. This will facilitate less manual interference in analysing complicated and rich patterns in data, and will be less prone to bias and estimation errors.

ACKNOWLEDGMENTS

We thank Rahul Sharma and J.C. Davis for sharing experimental data with us and for many helpful discussions that paved the course of the analysis presented in this work. We also thank Ilya Eremin, Marvin Müller, Miguel Sulangi, Roser Valentí and Karim Zantout for useful discussions. S.B. acknowledges support from the Deutsche Forschungsgemeinschaft (DFG, German Research Foundation) through TR 288-422213477. B. M. A. and A. T. R. acknowledge support from the Independent Research Fund Denmark grant number 8021-00047B. P.J.H. and S.B. acknowledge partial support from NSF-DMR-1849751.

Appendix A: First principles Wannier calculations

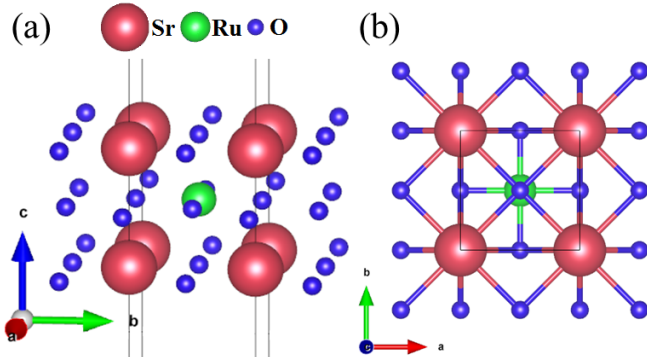


FIG. 5. (a) The supercell (constituent atoms and vacuum) of Sr_2RuO_4 depicted with black borders and constituent atoms Sr (maroon), Ru (green) and O (blue) as indicated by the color legend. The upper and lower extension of the supercell into vacuum has not been shown for brevity. Axis orientations are shown in the left-bottom corner. (b) Surface geometry of Sr_2RuO_4 when viewed above a certain height from the surface, with the Sr (maroon) and O (blue) atoms on very similar z -level. The bonds (in-plane and out-of-plane) between different atoms are depicted by the bi-colored lines.

Density functional theory calculations⁵⁶ were performed with the projected augmented wave (PAW) method as implemented in the Vienna ab initio simulation package (VASP)^{57,58}. The generalized gradient approximation of Perdew, Burke and Ernzerhof was used for the electron exchange correlation functional⁵⁹. To be able to capture the Wannier functions high above the surface we performed a monolayer calculation of perovskite Sr_2RuO_4 . The lattice constant was taken $a = 3.87\text{\AA}$, and the vacuum length was chosen to be about 21\AA .

Fig.5 provides the structural visualization of the crystal as used for the input of the *ab-initio* calculations. The energy cutoff of the plane waves was chosen as 650 eV. The total energy was converged to 10^{-7} eV. The Brillouin zone integration was sampled by using a $7 \times 7 \times 1$ Γ -centered Monkhorst-Pack grid. To construct the Wannier functions and the tight-binding models, the d_{xz} , d_{yz} and d_{xy} orbitals were projected on the low energy bands, employing the Wannier90 code package⁶⁰ with input parameters `num_iter` = 0 and `dis_num_iter` = 10000. The outer energy window was taken as $[-3, 1]$ eV and the inner frozen energy window as $[-1.7, 0.2]$ eV, both relative to the Fermi level. This Wannier function calculation is the same as was used in Ref. 51 for the case without surface reconstruction pertaining to the rotation of the Ru-O layer.

Appendix B: Representing pairing functions in orbitally-resolved Nambu basis:

The gap function obtained from Refs. [19 and 29] and illustrated in Fig.6 are typically expressed as a function of the normal state Fermi surface (FS) $\Delta_\mu(\mathbf{k}_F)$, where the gap magnitude tends to be the largest compared to the rest of the Brillouin zone (BZ). To obtain the gap function over the full BZ as required in Eq. (4), one can extrapolate its value from the μ -th Fermi band $\Delta_\mu(\mathbf{k}_F)$ as it falls off away from the FS, a behavior which can be parametrized in terms of a Gaussian-cutoff:

$$\Delta_\mu(\mathbf{k}) = \Delta_\mu(\mathbf{k}_F^{\text{nn}}) \exp\left(-(|E_\mu(\mathbf{k})|/\Delta_C)^2\right), \quad (\text{B1})$$

where $\Delta_C = 10\Delta_0$ and \mathbf{k}_F^{nn} refers to nearest-neighbor \mathbf{k}_F from \mathbf{k} . This provides a local picture of the internal orbital structure of a pair which continues out to a radius set by the coherence length ξ_0 . While implementing this extrapolation, one should keep in mind the translational invariance condition for the BZ, i.e. to obtain $\Delta_\mu(\mathbf{k})$ values in the 1st BZ $(-\pi/a : \pi/a)$, contributions of $\Delta_\mu(\mathbf{k}_F)$ values from the neighboring BZs $(-2\pi/a : 2\pi/a)$ should also be taken into account. The gap maxima value of $|\Delta_\mu(\mathbf{k})|$ in the BZ can also be set to a chosen Δ_0 , for instance, 3.5 meV for our numerical purpose. The following describes the next steps of basis transformation from bands to orbital basis, for representing the gap (pairing) functions.

1. Tight-binding Hamiltonian:

The non-interacting Hamiltonian $\hat{H}(\mathbf{k})$ as in Eq. (2) and Eq. (3), has the block diagonal structure:

$$\hat{H}(\mathbf{k}) = \begin{pmatrix} H_0(\mathbf{k}) + H_{\text{soc}}(+) & 0 \\ 0 & H_0(\mathbf{k}) + H_{\text{soc}}(-) \end{pmatrix}, \quad (\text{B2})$$

Since $H_{\text{soc}}(\sigma = \pm)$ has imaginary components, diagonalization of $\hat{H}(\mathbf{k})$ can yield eigenvectors that are linear

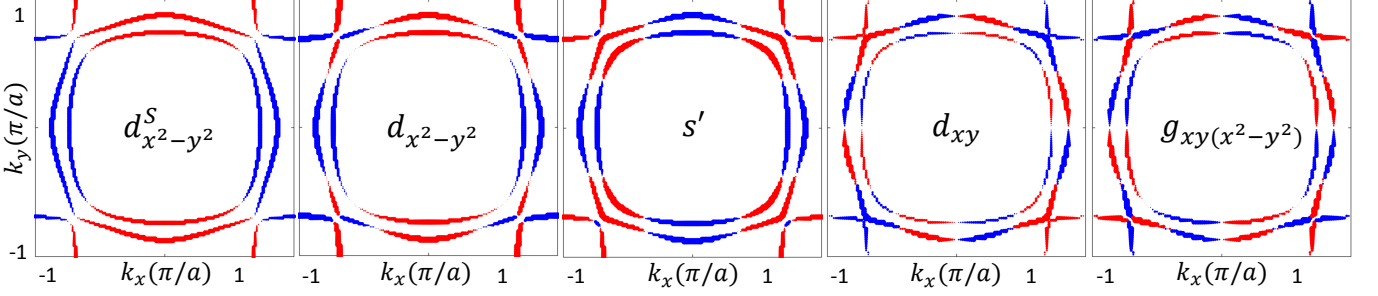


FIG. 6. Depictions of gap order parameters as a function of the Fermi surface for $d_{x^2-y^2}^S$ order parameter (simple intra-band form-factor of $\frac{\Delta_0}{2}(\cos k_x - \cos k_y)$), and the rest borrowed from Refs. [19 and 29] $d_{x^2-y^2}$, s' , d_{xy} and $g_{xy(x^2-y^2)}$. The red (blue) color denotes positive (negative) values of the order parameter and marker-size of each \mathbf{k}_F point is proportional to the gap magnitude $|\Delta(\mathbf{k})|$. Composite order parameters like $s' + id_{x^2-y^2}$, $s' + id_{xy}$ and $d_{x^2-y^2} + ig_{xy(x^2-y^2)}$ were obtained from complex combinations of the corresponding individual order parameters.

combination of Kramer's degenerate eigenstates owing to gauge-independence. To circumvent this, one can diagonalize $H_+(\mathbf{k}) = H_0(\mathbf{k}) + H_{\text{soc}}(+)$, and obtain unitary matrix $U^{(+)}(\mathbf{k})$ and then $H_-(\mathbf{k}) = H_0(\mathbf{k}) + H_{\text{soc}}(-)$, to obtain $U^{(-)}(\mathbf{k})$, and form the unitary matrix $U^{(0)}(\mathbf{k})$ such that:

$$U^{(0)}(\mathbf{k}) = \begin{pmatrix} U^{(+)}(\mathbf{k}) & 0 \\ 0 & U^{(-)}(\mathbf{k}) \end{pmatrix}, \quad (\text{B3})$$

$$U^{(0)\dagger}(\mathbf{k}) \hat{H}(\mathbf{k}) U^{(0)}(\mathbf{k}) = \begin{pmatrix} E^{(+)}(\mathbf{k}) & 0 \\ 0 & E^{(-)}(\mathbf{k}) \end{pmatrix}, \quad (\text{B4})$$

$U^{(0)}(\mathbf{k})$ diagonalizes $\hat{H}(\mathbf{k})$ to yield Kramer's degenerate pairs of eigenvalues $E^{(+)}(\mathbf{k}) = E^{(-)}(\mathbf{k})$.

2. Pairing function:

The gap part of the BCS Hamiltonian $\hat{\Delta}(\mathbf{k})$ is constructed in the same basis as the $\hat{H}(\mathbf{k})$. However, the gap values obtained from Eq. (B1) are represented in band pseudospin basis. For the three bands present in the Sr_2RuO_4 system and for singlet pairing with the Cooper-pair spin structure: $|\uparrow\downarrow\rangle - |\downarrow\uparrow\rangle$, we construct the gap matrix in this band pseudospin basis as $\Delta^{\text{pseudo}}(\mathbf{k})$:

$$\begin{pmatrix} \cdot & \cdot & \cdot & \Delta_1(\mathbf{k}) & \cdot & \cdot \\ \cdot & \cdot & \cdot & \cdot & \Delta_2(\mathbf{k}) & \cdot \\ \cdot & \cdot & \cdot & \cdot & \cdot & -\Delta_3(\mathbf{k}) \\ -\Delta_1(\mathbf{k}) & \cdot & \cdot & \cdot & \cdot & \cdot \\ \cdot & -\Delta_2(\mathbf{k}) & \cdot & \cdot & \cdot & \cdot \\ \cdot & \cdot & \Delta_3(\mathbf{k}) & \cdot & \cdot & \cdot \end{pmatrix}, \quad (\text{B5})$$

where the pseudospin-structure of the basis is $(\uparrow, \uparrow, \downarrow, \downarrow, \downarrow, \uparrow)$. One constructs the gap part of the Hamiltonian in the Nambu basis as

$$\hat{H}_\Delta = \begin{pmatrix} 0 & \Delta^{\text{pseudo}}(\mathbf{k}) \\ (\Delta^{\text{pseudo}}(\mathbf{k}))^\dagger & 0 \end{pmatrix}. \quad (\text{B6})$$

The unitary matrix in this Nambu basis

$$\underline{U}_N(\mathbf{k}) = \begin{pmatrix} U^{(0)}(\mathbf{k}) & 0 \\ 0 & (U^{(0)}(-\mathbf{k}))^* \end{pmatrix}, \quad (\text{B7})$$

that diagonalizes the non-interacting part of the Nambu Hamiltonian

$$\underline{\hat{H}}_N = \begin{pmatrix} \hat{H}(\mathbf{k}) & 0 \\ 0 & -\hat{H}^T(-\mathbf{k}) \end{pmatrix}, \quad (\text{B8})$$

can be applied on \hat{H}_Δ for unitary transformation from the band to orbital basis:

$$\underline{U}_N(\mathbf{k}) \hat{H}_\Delta(\mathbf{k}) \underline{U}_N^\dagger(\mathbf{k}) = \begin{pmatrix} 0 & \hat{\Delta}(\mathbf{k}) \\ \hat{\Delta}^\dagger(\mathbf{k}) & 0 \end{pmatrix}. \quad (\text{B9})$$

The matrix elements $\Delta_{mn}(\mathbf{k})$ of the block $\hat{\Delta}(\mathbf{k})$ are the orbitally resolved gap structure in the Nambu basis. Its real space representation is obtained by a simple Fourier transformation:

$$\Delta_{mn}(\mathbf{R}) = \frac{1}{N_k} \sum_{\mathbf{k}} \Delta_{mn}(\mathbf{k}) e^{-i\mathbf{k}\cdot\mathbf{R}}, \quad (\text{B10})$$

where \mathbf{R} refers to different lattice sites centered around (0,0). The amplitude $\Delta_{mn}(\mathbf{R})$ encodes the internal spatial and orbital structures of the electron pair. With the information of $\Delta_{mn}(\mathbf{R})$ and its simple inverse Fourier transformation back to momentum-space, one can set up the full BCS Hamiltonian of Eq. (4) in combination with any tight binding parameters.

Appendix C: Detailed description of the analysis of the BQPI patterns for ranking the different gap order parameters:

In this section, we describe the score assignment procedure for ranking the different order parameters as per their BQPI pattern matching with the experiments. As mentioned earlier, we identified 4 \mathbf{q} -positions from their

Gap order	Colored circle or feature	$ \omega /\Delta = 0$	$ \omega /\Delta = 0.26$	$ \omega /\Delta = 0.58$	$ \omega /\Delta = 0.84$	Total score out of 16
Experimental features	Red	Diagonally elongated stripes	Diagonally elongated stripes	Diagonally elongated stripes	Diagonally elongated stripes	
	Green	+Y-pointed triangle	+Y-pointed triangle	+Y-pointed triangle	+Y-pointed triangle	
	Blue	\pm Y-elongated stripe	\pm Y-elongated stripe	\pm Y-elongated stripe	Sharp peak	
	Yellow	-Y-pointed triangle	Dispersing triangle	Dispersing triangle	Dispersing triangle	
	Enhanced edges at $\pm 1.5\pi/a$	No	No	Yes	Yes	
$s' + id_{xy}$	Red	1	1	1	1	
	Green	1	1	1	1	
	Blue	1	1	0	1	14
	Yellow	1	0	1	1	
	Enhanced edges	No	No	Yes	Yes	
$s' + id_{x^2-y^2}$	Red	1	1	1	0	
	Green	1	1	1	1	
	Blue	0	0	1	1	11
	Yellow	0	0	1	1	
	Enhanced edges	Yes	No	Yes	Yes	
$d_{x^2-y^2}^S$	Red	1	1	1	1	
	Green	1	1	1	1	
	Blue	0	1	0	0	11
	Yellow	1	1	0	0	
	Enhanced edges	Yes	No	No	Yes	
s'	Red	1	1	1	0	
	Green	1	1	1	1	
	Blue	0	0	0	0	9
	Yellow	1	0	0	1	
	Enhanced edges	No	No	No	Yes	
$d_{x^2-y^2}$	Red	1	1	0	0	
	Green	1	1	1	1	
	Blue	0	0	1	0	8
	Yellow	1	0	0	0	
	Enhanced edges	Yes	No	Yes	No	
$d_{x^2-y^2} + ig_{xy}(x^2-y^2)$	Red	1	1	1	0	
	Green	1	1	1	1	
	Blue	0	0	0	1	8
	Yellow	0	0	0	0	
	Enhanced edges	No	No	Yes	Yes	

TABLE II. A detailed score chart summarizing the correspondence of the four specific \mathbf{q} -features at the colored circles (see Fig.4) between experimental and theoretically evaluated BQPI maps, for various gap order parameters across all STM biases $|\omega|/\Delta$. The first row mentions the specific BQPI features that were identified in the experimental data. In the following rows corresponding to specific gap order parameters, individual scores are denoted by 1 or 0, based on whether there's a pattern matching or deviation between experimental and numerical results within each colored circle. The cumulative total score out of 16 \mathbf{q} -features (4 \mathbf{q} -features across 4 bias values) determines the ranking for the correspondence of the individual gap order parameters when matched with experimental BQPI patterns. Additional qualitative feature of having enhanced edges at $\pm 1.5\pi/a$ have also been shown with a binary 'Yes/No' score.

ubiquitous and robust presence across all STM bias values in the experimental BQPI maps and marked them in red, green, blue and yellow colored circles (see Fig.4, first row). The specific BQPI patterns within these circles are identified as follows: (red) diagonally elongated

stripes, (green) triangle pointed along $+q_y$ direction, (blue) stripe elongated along $\pm q_y$ direction and (yellow) triangle pointed along $-q_y$ direction. For assigning a score to our numerical predictions, a good match between the experimental pattern and our numerical predictions

within each specific colored circle was assigned a score of 1, and deviations were assigned a score of 0. Table II quantifies the details of this analysis with rankings shown in descending order as before. An additional experimental feature is the enhanced intensities along the square edges positioned around $(\pm 1.5\pi/a)$ at higher STM biases $|\omega|/\Delta = [0.58, 0.84]$ as opposed to the lower biases $|\omega|/\Delta = [0, 0.26]$. These feature has been ranked qual-

itatively (binary ‘Yes’ or ‘No’ score) in our score chart with $s' + id_{xy}$ displaying the best match with this trend, while other order parameters displays a different trend.

Although our approach is highly subjective in nature, unfortunately, we do not have a more quantitative way to approach this pattern-matching problem. We are restricted by the limited availability of experimental data at ultra-low temperatures.

¹ Andrew Peter Mackenzie and Yoshiteru Maeno, “The superconductivity of Sr_2RuO_4 and the physics of spin-triplet pairing,” *Rev. Mod. Phys.* **75**, 657–712 (2003).

² Yoshiteru Maeno, Shunichiro Kittaka, Takuji Nomura, Shingo Yonezawa, and Kenji Ishida, “Evaluation of spin-triplet superconductivity in Sr_2RuO_4 ,” *Journal of the Physical Society of Japan* **81**, 011009 (2012).

³ Catherine Kallin and John Berlinsky, “Chiral superconductors,” *Reports on Progress in Physics* **79**, 054502 (2016).

⁴ Andrew P. Mackenzie, Thomas Scaffidi, Clifford W. Hicks, and Yoshiteru Maeno, “Even odder after twenty-three years: the superconducting order parameter puzzle of Sr_2RuO_4 ,” *npj Quantum Materials* **2** (2017).

⁵ K. Ishida, H. Mukuda, Y. Kitaoka, K. Asayama, Z. Q. Mao, Y. Mori, and Y. Maeno, “Spin-triplet superconductivity in Sr_2RuO_4 identified by ^{17}O Knight shift,” *Nature* **396**, 658–660 (1998).

⁶ G. M. Luke, Y. Fudamoto, K. M. Kojima, M. I. Larkin, J. Merrin, B. Nachumi, Y. J. Uemura, Y. Maeno, Z. Q. Mao, Y. Mori, H. Nakamura, and M. Sigrist, “Time-reversal symmetry-breaking superconductivity in Sr_2RuO_4 ,” *Nature* **394**, 558–561 (1998).

⁷ Jing Xia, Yoshiteru Maeno, Peter T. Beyersdorf, M. M. Fejer, and Aharon Kapitulnik, “High resolution polar kerr effect measurements of Sr_2RuO_4 : Evidence for broken time-reversal symmetry in the superconducting state,” *Phys. Rev. Lett.* **97**, 167002 (2006).

⁸ T M Rice and M Sigrist, “ Sr_2RuO_4 : an electronic analogue of 3He ?” *Journal of Physics: Condensed Matter* **7**, L643–L648 (1995).

⁹ I. Bonalde, Brian D. Yanoff, M. B. Salamon, D. J. Van Harlingen, E. M. E. Chia, Z. Q. Mao, and Y. Maeno, “Temperature dependence of the penetration depth in Sr_2RuO_4 : Evidence for nodes in the gap function,” *Phys. Rev. Lett.* **85**, 4775–4778 (2000).

¹⁰ Shuji NishiZaki, Yoshiteru Maeno, and Zhiqiang Mao, “Changes in the superconducting state of Sr_2RuO_4 under magnetic fields probed by specific heat,” *Journal of the Physical Society of Japan* **69**, 572–578 (2000).

¹¹ K. Deguchi, Z. Q. Mao, H. Yaguchi, and Y. Maeno, “Gap structure of the spin-triplet superconductor Sr_2RuO_4 determined from the field-orientation dependence of the specific heat,” *Phys. Rev. Lett.* **92**, 047002 (2004).

¹² E. Hassinger, P. Bourgeois-Hope, H. Taniguchi, S. René de Cotret, G. Grissonnanche, M. S. Anwar, Y. Maeno, N. Doiron-Leyraud, and Louis Taillefer, “Vertical line nodes in the superconducting gap structure of Sr_2RuO_4 ,” *Phys. Rev. X* **7**, 011032 (2017).

¹³ A. Pustogow, Yongkang Luo, A. Chronister, Y.-S. Su, D. A. Sokolov, F. Jerzembeck, A. P. Mackenzie, C. W. Hicks, N. Kikugawa, S. Raghu, and et al., “Constraints on the superconducting order parameter in Sr_2RuO_4 from oxygen-17 nuclear magnetic resonance,” *Nature* **574**, 72–75 (2019).

¹⁴ Kenji Ishida, Masahiro Manago, Katsuki Kinjo, and Yoshiteru Maeno, “Reduction of the ^{17}O Knight Shift in the Superconducting State and the Heat-up Effect by NMR Pulses on Sr_2RuO_4 ,” *Journal of the Physical Society of Japan* **89**, 034712 (2020).

¹⁵ Aaron Chronister, Andrej Pustogow, Naoki Kikugawa, Dmitry A. Sokolov, Fabian Jerzembeck, Clifford W. Hicks, Andrew P. Mackenzie, Eric D. Bauer, and Stuart E. Brown, “Evidence for even parity unconventional superconductivity in Sr_2RuO_4 ,” *Proceedings of the National Academy of Sciences* **118** (2021).

¹⁶ S. Benhabib, C. Lupien, I. Paul, L. Berges, M. Dion, M. Nardone, A. Zitouni, Z. Q. Mao, Y. Maeno, A. Georges, and et al., “Ultrasound evidence for a two-component superconducting order parameter in Sr_2RuO_4 ,” *Nature Physics* **17**, 194–198 (2020).

¹⁷ Sayak Ghosh, Arkady Shekhter, F. Jerzembeck, N. Kikugawa, Dmitry A. Sokolov, Manuel Brando, A. P. Mackenzie, Clifford W. Hicks, and B. J. Ramshaw, “Thermodynamic evidence for a two-component superconducting order parameter in Sr_2RuO_4 ,” *Nature Physics* (2020).

¹⁸ Vadim Grinenko, Shreenanda Ghosh, Rajib Sarkar, Jean-Christophe Orain, Artem Nikitin, Matthias Elender, Debarchan Das, Zurab Guguchia, Felix Brückner, Mark E. Barber, Joonbum Park, Naoki Kikugawa, Dmitry A. Sokolov, Jake S. Bobowski, Takuto Miyoshi, Yoshiteru Maeno, Andrew P. Mackenzie, Hubertus Luetkens, Clifford W. Hicks, and Hans-Henning Klauss, “Split superconducting and time-reversal symmetry-breaking transitions in Sr_2RuO_4 under stress,” *Nature Physics* **17**, 748–754 (2021).

¹⁹ A. T. Rømer, D. D. Scherer, I. M. Eremin, P. J. Hirschfeld, and B. M. Andersen, “Knight shift and leading superconducting instability from spin fluctuations in Sr_2RuO_4 ,” *Phys. Rev. Lett.* **123**, 247001 (2019).

²⁰ Henrik S. Røsing, Thomas Scaffidi, Felix Flicker, Gunnar F. Lange, and Steven H. Simon, “Superconducting order of Sr_2RuO_4 from a three-dimensional microscopic model,” *Phys. Rev. Research* **1**, 033108 (2019).

²¹ O. Gingras, R. Nourafkan, A.-M. S. Tremblay, and M. Côté, “Superconducting symmetries of Sr_2RuO_4 from first-principles electronic structure,” *Phys. Rev. Lett.* **123**, 217005 (2019).

²² Han Gyeol Suh, Henri Menke, P. M. R. Brydon, Carsten Timm, Aline Ramires, and Daniel F. Agterberg, “Stabilizing even-parity chiral superconductivity in Sr_2RuO_4 ,” *Phys. Rev. Research* **2**, 032023 (2020).

²³ S.-O. Kaba and D. Sénéchal, “Group-theoretical classifi-

cation of superconducting states of strontium ruthenate," *Phys. Rev. B* **100**, 214507 (2019).

²⁴ Aline Ramires and Manfred Sigrist, "Superconducting order parameter of Sr_2RuO_4 : A microscopic perspective," *Phys. Rev. B* **100**, 104501 (2019).

²⁵ Swagata Acharya, Dimitar Pashov, Cédric Weber, Hyowon Park, Lorenzo Sponza, and Mark Van Schilfgaarde, "Evening out the spin and charge parity to increase T_c in Sr_2RuO_4 ," *Communications Physics* **2**, 163 (2019).

²⁶ Zhiqiang Wang, Xin Wang, and Catherine Kallin, "Spin-orbit coupling and spin-triplet pairing symmetry in Sr_2RuO_4 ," *Phys. Rev. B* **101**, 064507 (2020).

²⁷ Astrid T. Rømer, Andreas Kreisel, Marvin A. Müller, P. J. Hirschfeld, Ilya M. Eremin, and Brian M. Andersen, "Theory of strain-induced magnetic order and splitting of T_c and $T_{\text{trs}b}$ in Sr_2RuO_4 ," *Phys. Rev. B* **102** (2020).

²⁸ A. T. Rømer and B. M. Andersen, "Fluctuation-driven superconductivity in Sr_2RuO_4 from weak repulsive interactions," *Modern Physics Letters B* **34**, 2040052 (2020).

²⁹ Astrid T. Rømer, P. J. Hirschfeld, and Brian M. Andersen, "Superconducting state of Sr_2RuO_4 in the presence of longer-range Coulomb interactions," *Phys. Rev. B* **104**, 064507 (2021).

³⁰ Steven Allan Kivelson, Andrew Chang Yuan, Brad Ramshaw, and Ronny Thomale, "A proposal for reconciling diverse experiments on the superconducting state in Sr_2RuO_4 ," *npj Quantum Materials* **5** (2020).

³¹ Jonathan Clepkens, Austin W. Lindquist, and Hae-Young Kee, "Shadowed triplet pairings in Hund's metals with spin-orbit coupling," *Phys. Rev. Research* **3**, 013001 (2021).

³² Roland Willa, Matthias Hecker, Rafael M. Fernandes, and Jörg Schmalian, "Inhomogeneous time-reversal symmetry breaking in Sr_2RuO_4 ," *Phys. Rev. B* **104**, 024511 (2021).

³³ Fabian B. Kugler, Manuel Zingl, Hugo U. R. Strand, Seung-Sup B. Lee, Jan von Delft, and Antoine Georges, "Strongly correlated materials from a numerical renormalization group perspective: How the Fermi-liquid state of Sr_2RuO_4 emerges," *Phys. Rev. Lett.* **124**, 016401 (2020).

³⁴ Jernej Mravlje, Markus Aichhorn, Takashi Miyake, Kristjan Haule, Gabriel Kotliar, and Antoine Georges, "Coherence-Incoherence Crossover and the Mass-Renormalization Puzzles in Sr_2RuO_4 ," *Phys. Rev. Lett.* **106**, 096401 (2011).

³⁵ M. W. Haverkort, I. S. Elfimov, L. H. Tjeng, G. A. Sawatzky, and A. Damascelli, "Strong spin-orbit coupling effects on the Fermi surface of Sr_2RuO_4 and Sr_2RhO_4 ," *Phys. Rev. Lett.* **101**, 026406 (2008).

³⁶ Minjae Kim, Jernej Mravlje, Michel Ferrero, Olivier Parcollet, and Antoine Georges, "Spin-orbit coupling and electronic correlations in Sr_2RuO_4 ," *Phys. Rev. Lett.* **120**, 126401 (2018).

³⁷ S. Raghu, A. Kapitulnik, and S. A. Kivelson, "Hidden quasi-one-dimensional superconductivity in Sr_2RuO_4 ," *Phys. Rev. Lett.* **105**, 136401 (2010).

³⁸ Thomas Scaffidi, Jesper C. Romers, and Steven H. Simon, "Pairing symmetry and dominant band in Sr_2RuO_4 ," *Phys. Rev. B* **89**, 220510 (2014).

³⁹ S. Benhabib, C. Lupien, I. Paul, L. Berges, M. Dion, M. Nardone, A. Zitouni, Z. Q. Mao, Y. Maeno, A. Georges, L. Taillefer, and C. Proust, "Ultrasound evidence for a two-component superconducting order parameter in Sr_2RuO_4 ," *Nature Physics* **17**, 194–198 (2021).

⁴⁰ I. A. Firmino, S. Lederer, C. Lupien, A. P. Mackenzie, J. C. Davis, and S. A. Kivelson, "Evidence from tunneling spectroscopy for a quasi-one-dimensional origin of superconductivity in Sr_2RuO_4 ," *Phys. Rev. B* **88**, 134521 (2013).

⁴¹ Rahul Sharma, Stephen D. Edkins, Zhenyu Wang, Andrei Kostin, Chanchal Sow, Yoshiteru Maeno, Andrew P. Mackenzie, J. C. Séamus Davis, and Vidya Madhavan, "Momentum-resolved superconducting energy gaps of Sr_2RuO_4 from quasiparticle interference imaging," *Proceedings of the National Academy of Sciences* **117**, 5222–5227 (2020).

⁴² T. Hanaguri, Y. Kohsaka, J. C. Davis, C. Lupien, I. Yamada, M. Azuma, M. Takano, K. Ohishi, M. Ono, and H. Takagi, "Quasiparticle interference and superconducting gap in $\text{Ca}_{2-x}\text{Na}_x\text{CuO}_2\text{Cl}_2$," *Nature Physics* **3**, 865–871 (2007).

⁴³ M. P. Allan, A. W. Rost, A. P. Mackenzie, Yang Xie, J. C. Davis, K. Kihou, C. H. Lee, A. Iyo, H. Eisaki, and T.-M. Chuang, "Anisotropic energy gaps of iron-based superconductivity from intraband quasiparticle interference in LiFeAs ," *Science* **336**, 563–567 (2012).

⁴⁴ P. O. Sprau, A. Kostin, A. Kreisel, A. E. Böhmer, V. Taufour, P. C. Canfield, S. Mukherjee, P. J. Hirschfeld, B. M. Andersen, and J. C. Séamus Davis, "Discovery of orbital-selective cooper pairing in FeSe ," *Science* **357**, 75–80 (2017).

⁴⁵ Satoshi Kashiwaya, Kohta Saitoh, Hiromi Kashiwaya, Masao Koyanagi, Masatoshi Sato, Keiji Yada, Yukio Tanaka, and Yoshiteru Maeno, "Time-reversal invariant superconductivity of Sr_2RuO_4 revealed by Josephson effects," *Phys. Rev. B* **100**, 094530 (2019).

⁴⁶ A. Kreisel, Peayush Choubey, T. Berlijn, W. Ku, B. M. Andersen, and P. J. Hirschfeld, "Interpretation of scanning tunneling quasiparticle interference and impurity states in cuprates," *Phys. Rev. Lett.* **114**, 217002 (2015).

⁴⁷ A. Kreisel, R. Nelson, T. Berlijn, W. Ku, Ramakrishna Aluru, Shun Chi, Haibiao Zhou, Udai Raj Singh, Peter Wahl, Ruixing Liang, Walter N. Hardy, D. A. Bonn, P. J. Hirschfeld, and Brian M. Andersen, "Towards a quantitative description of tunneling conductance of superconductors: Application to LiFeAs ," *Phys. Rev. B* **94**, 224518 (2016).

⁴⁸ V.B. Zabolotnyy, D.V. Evtushinsky, A.A. Kordyuk, T.K. Kim, E. Carleschi, B.P. Doyle, R. Fittipaldi, M. Cuoco, A. Vecchione, and S.V. Borisenko, "Renormalized band structure of Sr_2RuO_4 : A quasiparticle tight-binding approach," *Journal of Electron Spectroscopy and Related Phenomena* **191**, 48–53 (2013).

⁴⁹ Sergio Cobo, Felix Ahn, Ilya Eremin, and Alireza Akbari, "Anisotropic spin fluctuations in Sr_2RuO_4 : Role of spin-orbit coupling and induced strain," *Phys. Rev. B* **94** (2016).

⁵⁰ Jennifer E Hoffman, "Spectroscopic scanning tunneling microscopy insights into Fe-based superconductors," *Reports on Progress in Physics* **74**, 124513 (2011).

⁵¹ A. Kreisel, C. A. Marques, L. C. Rhodes, X. Kong, T. Berlijn, R. Fittipaldi, V. Granata, A. Vecchione, P. Wahl, and P. J. Hirschfeld, "Unveiling the missing band: Quasiparticle interference of the γ -band in Sr_2RuO_4 ," (2021), [arXiv:2103.06188 \[cond-mat.str-el\]](https://arxiv.org/abs/2103.06188).

⁵² I. A. Firmino, S. Lederer, C. Lupien, A. P. Mackenzie, J. C. Davis, and S. A. Kivelson, "Evidence from tunneling spectroscopy for a quasi-one-dimensional origin of superconductivity in Sr_2RuO_4 ," *Phys. Rev. B* **88**, 134521 (2013).

⁵³ Zhenyu Wang, Daniel Walkup, Philip Derry, Thomas Scaf-

fidi, Melinda Rak, Sean Vig, Anshul Kogar, Ilija Zeljkovic, Ali Husain, Luiz H. Santos, and et al., “Quasiparticle interference and strong electron-mode coupling in the quasi-one-dimensional bands of Sr_2RuO_4 ,” *Nature Physics* **13**, 799–805 (2017).

⁵⁴ K. McElroy, R. W. Simmonds, J. E. Hoffman, D. H. Lee, J. Orenstein, H. Eisaki, S. Uchida, and J. C. Davis, “Relating atomic-scale electronic phenomena to wave-like quasiparticle states in superconducting $\text{Bi}_2\text{Sr}_2\text{CaCu}_2\text{O}_{8+\delta}$,” *Nature* **422**, 592–596 (2003).

⁵⁵ Yi Zhang, A. Mesaros, K. Fujita, S. D. Edkins, M. H. Hamidian, K. Ch’ng, H. Eisaki, S. Uchida, J. C. Séamus Davis, Ehsan Khatami, and Eun-Ah Kim, “Machine learning in electronic-quantum-matter imaging experiments,” *Nature* **570**, 484–490 (2019).

⁵⁶ P. Hohenberg and W. Kohn, “Inhomogeneous electron gas,” *Phys. Rev.* **136**, B864–B871 (1964).

⁵⁷ G. Kresse and J. Furthmüller, “Efficient iterative schemes for ab initio total-energy calculations using a plane-wave basis set,” *Phys. Rev. B* **54**, 11169–11186 (1996).

⁵⁸ G. Kresse and D. Joubert, “From ultrasoft pseudopotentials to the projector augmented-wave method,” *Phys. Rev. B* **59**, 1758–1775 (1999).

⁵⁹ John P. Perdew, Kieron Burke, and Matthias Ernzerhof, “Generalized gradient approximation made simple,” *Phys. Rev. Lett.* **77**, 3865–3868 (1996).

⁶⁰ Arash A. Mostofi, Jonathan R. Yates, Young-Su Lee, Ivo Souza, David Vanderbilt, and Nicola Marzari, “Wannier90: A tool for obtaining maximally-localised Wannier functions,” *Computer Physics Communications* **178**, 685–699 (2008).